Progress in Organic Coatings 134 (2019) 272–280

Contents lists available at ScienceDirect

Progress in Organic Coatings

journal homepage: www.elsevier.com/locate/porgcoat

# Size-dependent corrosion behavior of graphene oxide coating

Nurul Huda Abu Bakar[a], Gomaa A.M. Ali[a,b], Jamil Ismail[a], H. Algarni[c,d], Kwok Feng Chong[a,*]

[a] Faculty of Industrial Sciences & Technology, Universiti Malaysia Pahang, Gambang, 26300, Kuantan, Malaysia
[b] Chemistry Department, Faculty of Science, Al–Azhar University, Assiut, 71524, Egypt
[c] Research Centre for Advanced Materials Science (RCAMS), King Khalid University, Abha, 61413, P. O. Box 9004, Saudi Arabia
[d] Department of Physics, Faculty of Sciences, King Khalid University, P. O. Box 9004, Abha, Saudi Arabia

ARTICLE INFO

*Keywords:*
Sheet size
Coating
Electrodeposition
EIS
Corrosion protection

ABSTRACT

Graphene oxide emerges as an effective corrosion resistant coating. However, the influence of graphene oxide sheets size on the corrosion protection remains unclear. In this report, we investigate the effect of different graphene oxide (GO) sheets size in the formation of corrosion resistant coating. We provide valuable input for electrophoretic deposition in which GO sheets in smaller size diffuse faster during deposition to cause more oxygen reduction, thereby forms a coating with higher hydrophobicity, stronger adhesion, and lesser pinholes. Detailed electrochemical impedance analysis shows that the coating formed from GO sheets in smaller size exhibits higher activation energy for water diffusion, causing slower water diffusion rate and lower permeation into the coating. The findings suggest that GO sheets in smaller size produce a reliable coating with excellent corrosion resistance behavior.

## 1. Introduction

Corrosion in metallic materials is inevitable due to the occurrence of chemical or electrochemical reactions when they are in contact with moisture/water, acids, bases, salts or other aggressive chemicals. Proper corrosion prevention protocols are needed to minimize various severe damages for the material resources preservation and economy loss prevention. It has been reported that the use of corrosion inhibitors successfully interrupt the corrosion process by the formation of a passive layer due to the interaction between inhibitors' functional groups and metallic surfaces [1–3]. Current researches have found that green corrosion inhibitors such as orange peel extract [4], watermelon rind extract [5] and *Plantago* containing polysaccharide [6] as well as ascorbic acids [7] can control the diffusion of corrosive ions onto the metal surface. However, the compatibility and stability of the corrosion inhibitors in the corrosion system might constraint the efficiency of the inhibitors.

Alternatively, coatings can be applied to the metal surface as a protective barrier to delay the corrosion process. It can enhance the surface properties that the materials do not have prior to the coating. A protective coating can either be sprayed by cold [8] or plasma [9] spraying technique and even plated [10] on the metal surface. In recent years, electrophoretic deposition or EPD has been adopted to fabricate the protective coating due to its high versatility [11–13]. Basically, EPD requires the use of an electric field to impel the suspended particles in a colloidal system for substrate deposition. The advantages of EPD technique are, but not limited to short deposition time, simple set up, low cost and applicable to various shapes and sizes of a substrate. The film thickness and morphology can also be manipulated by adjusting the EPD time and voltage [14].

There are increasing publications reports on the assistance of EPD in the fabrication of graphene and its derivatives coatings [15–18]. The EPD graphene coating is said to have excellent electrical conductivity, optical transparency, large surface area and desirable mechanical properties [13,19]. In most cases, the EPD of pure graphene on the metallic surface requires the addition of surfactants or additives due to its poor dispersibility in aqueous solution [20–22]. As an alternative, deposition from the colloidal suspension of graphene oxide (GO) is preferred because of its high dispersibility from a large number of oxygenated functional groups (epoxide, hydroxyl, carboxyl and carbonyl) [2,23,24]. Generally, the anodic EPD process is conducted on GO due to its negative charging nature in the colloidal suspension. An et al. suggested that reduction occurred during the anodic EPD of GO in which partially reduced graphene oxide was formed on the surface of anode [25]. A recent study by Raza et al. showed that the anodic EPD-GO coating successfully reduced the corrosion rate of Cu metal in 0.6 M NaCl by approximately 6-times, as compared to the bare Cu [26]. Ho et al. also reported that the EPD-GO coating on steel substrate could provide superior barrier effect in the 3.5% NaCl solution towards corrosion activity [27]. Park et al. revealed that the EPD of GO layers

* Corresponding author.
*E-mail address:* ckfeng@ump.edu.my (K.F. Chong).

https://doi.org/10.1016/j.porgcoat.2019.05.011
Received 22 February 2019; Received in revised form 17 April 2019; Accepted 8 May 2019

underneath the top organic coating on steel effectively blocked the permeation of oxygen and water, thereby suppressed the cathodic reaction for corrosion [28].

The ultimate performance of EPD-GO coating is closely related to the adhesion, microtexture and surface roughness of the GO coating [29]. The GO sheets size is expected to be a key factor in the EPD process as the edges of a GO sheet (mainly decorated by oxygenated functional groups) are believed to be more active than the $sp^2$-hybridized basal planes [30,31]. The previous studies showed that different GO sheets sizes could be produced by varying the sonication time in the GO preparation [32,33], and possibly produced GO up to nano size [34]. The investigation on the relationship between GO sheets size for EPD process and the electrochemical performance of the coating is essential for the development of corrosion resistant EPD-GO coating. It will provide a new concept on the EPD process of GO, stimulate scientific insight of the EPD-GO coating and also benefit further applications toward metal protection in various industries.

In this contribution, EPD-GO coatings were prepared by electrodeposition of GO in different sheets sizes that were produced at different ultrasonication time. The differences in coating microtexture, surface chemistry and the relationship between them and the corrosion resistance behavior were systematically investigated.

## 2. Experimental section

### 2.1. Materials and GO synthesis

All chemicals used in this research were of analytical grade and were obtained from Sigma–Aldrich unless otherwise specified. Flat copper strips were purchased from Kimberly RD, Hong Kong, with 99.9% purity and dimension of 0.1 × 1.0 × 4.0 cm. Before EPD, all substrates were cleaned with acetone in an ultrasonic bath and dried at room temperature.

GO were synthesized *via* modified Hummers' method [35]. Graphite flakes (4.0 g) was first put into a mixture of conc. $H_2SO_4$ (30 mL), $K_2S_2O_8$ (6.0 g) and $P_2O_5$ (6.0 g) for pre-oxidation. The mixture was put in a round-bottomed flask and stirred homogeneously for 6 h at 80 °C with a thermo-coupled hotplate. It was then cooled to room temperature, followed by the addition of 2 L of deionized (DI) water and the pre-oxidized graphite was obtained after filtration. The obtained product was then dried in vacuum. After completely dried, the pre-oxidized graphite (~4.0 g) was put into 300 mL conc. $H_2SO_4$ and was transferred to an ice bath under magnetic stirring. Then, $KMnO_4$ (35.0 g) was added gradually, and the temperature of the mixture was kept at below 20 °C. Successively, the mixture was transferred to an oil bath and continued stirring at 35 °C for 4 h before diluting with 900 mL DI water. After that, 100 mL 30% $H_2O_2$ was added drop by drop and the mixture was filtered and washed with DI water and HCl (2 L) based on a volume ratio 10:1 to remove the residual ions [36,37]. The process was continued by centrifugation at 10 000 rpm in DI water for 20 min. The centrifugation and washing were repeated until the mixture became neutral in pH. Finally, GO was obtained after freeze-drying process.

### 2.2. Ultrasonication and electrophoretic deposition

The as-synthesized GO was first dispersed in DI water to make up a concentration of 1.0 mg/mL. The GO dispersion was then divided into two different vials for 1 h and 7 h ultrasonication using Bransonic CPX2800H (110 W, 40 kHz) to yield GO in different sheets sizes. They were termed as 1h-GO and 7h-GO throughout the discussion. Both were centrifuged at 6000 rpm before the EPD process in order to remove any un-exfoliated GO.

A two-electrode system was used for EPD with both anode and cathode were made of copper strips. A potentiostat (PGSTAT101; Autolab) was used for the EPD process to supply 1.0 V for 900 s until a uniform coating was obtained. A higher or lower deposition time resulted in the uneven and peeled-off coating. All of the EPD-GO samples were dried in an oven at 80 °C, overnight. Hereafter the EPD-GO coatings were labeled as 1h-GO/Cu and 7h-GO/Cu for the coating formed from 1h-GO and 7h-GO, respectively.

### 2.3. Characterizations

The functional groups of the samples were determined by Fourier Transform Infrared Spectrometer (FTIR; Spectrum 100 by Perkin Elmer), in the range of 400 – 4000 $cm^{-1}$. The graphitic structure and crystallinity of the samples were investigated by Raman spectrometer (inVia Reflex by Renishaw) with 532 nm laser light source and X-ray Diffractometer (XRD; Miniflex II by Rigaku). The GO sheets size distribution and their morphology were observed by field emission scanning electron microscope (FESEM; JSM-7800 F by JEOL) at 5.0 kV. Atomic force microscope (AFM; SPA 400 equipped with an SPI-3800 controller by Seiko Instruments) was used to study the surface of 10 × 10 μm at 0.30 Hz scan rate. The coating thickness was measured by a surface profiler (P-6 Stylus Profiler by KLA Tencor). The coating toughness and adhesion were evaluated by a surface indenter (Rockwell 574 by Wilson Instrument). Triplicate measurements were conducted to ensure results' accuracy.

### 2.4. Corrosion study

The corrosion performance of 1h-GO/Cu and 7h-GO/Cu coatings were evaluated using Tafel polarization curves. The corrosion tests were performed by a potentiostat (PGSTAT101; Autolab) in the three-electrode electrochemical cell, immersed in 3.5% NaCl solution with Ag/AgCl as a reference electrode and platinum wire as a counter electrode. The working electrode, with 1 $cm^2$ exposed area was stabilized at open circuit potential (OCP) at which its fluctuation was less than 50 μV for a period of 1000s. All assembled electrodes were separated at 1 cm apart throughout the experiment. The polarization curves were measured immediately after the OCP at a scan rate of 1 mV/s within scan range of -250 to +250 mV. The corrosion potential ($E_{corr}$) and corrosion current density ($I_{corr}$) were determined from the Tafel polarization curve. Electrochemical impedance spectroscopy (EIS) analysis was carried out in the same test solution with a frequency range from 10 mHz to 100 kHz at 10 mV amplitude voltage.

## 3. Results and discussion

### 3.1. Characterization of GO sheets

The first criterion to be investigated after the ultrasonication process is lateral size distribution. 150 GO sheets were counted during FESEM imaging, and the length along the diagonal direction of the sheets was measured and shown in Fig. 1. The mean lateral size for samples 1h-GO and 7h-GO are found to be 290 and 100 nm, respectively. The decrease in the mean lateral size indicates that prolonged ultrasonication time promotes GO fragmentation into smaller sheets. This is due to the increment of local temperature and pressure during sonication that facilitate fragmentation at the atomic level [38]. In addition, the presence of oxygen functional groups on the basal plane creates the weak points that could contribute to the break-up of the graphene sheets when sonicated for a long time [39–41]. Meanwhile, it was reported that sonication induced the separation layers of graphite oxide as well as the fractured of sheets into a smaller size [42,43].

The reaction at the atomic level also changes the GO chemical structure dynamically due to the rupture of chemical bonds as shown in FTIR results (Fig. S1). A significant reduction on the absorptions of O—H stretching vibration at *ca.* 3416 $cm^{-1}$ and C═O stretching vibration at *ca.* 1710 $cm^{-1}$ is observed with the decrease of the size of the sheets [37,44]. However, the absorption band of scissoring stretching of $-CH_2$ at 1470 $cm^{-1}$ is increased after prolonged ultrasonication time.

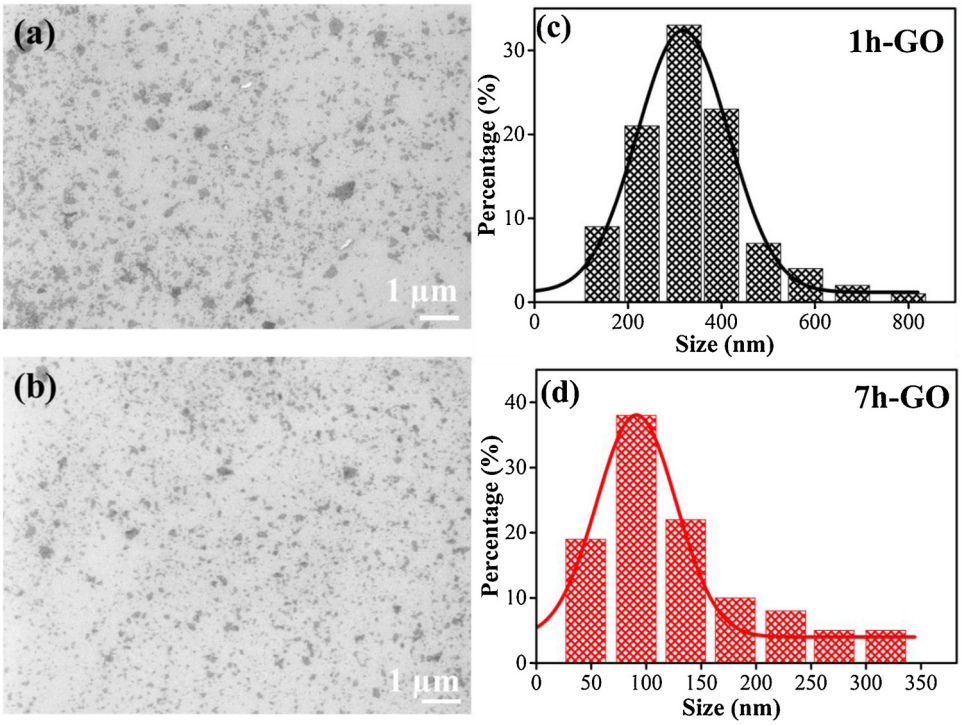


**Fig. 1.** Comparison of FESEM images (a, b) and size distribution (c, d) of GO sheets at 1h-GO and 7h-GO.

Gonçalves et al. suggested a mechanism during the fragmentation process as Confined Hot Spot Atomic Reduction [34]. The process begins with the propagation of cracks over the defect zones, followed by the elimination of oxygen functional groups (COOH and C═O), thereby forming $-CH_2$ bonds, that increase the hydrophobicity.

Quantitative analysis of oxygen-related band (ORB) [45] was determined from the FTIR spectra. The ORB determination is useful for the oxygen contents estimation. It is found that ORB for 1h-GO is 0.70 which is slightly higher as compared to 0.65 for 7h-GO. The value is in agreement with the fact that prolonged ultrasonication time facilitates the elimination of oxygen functional groups by decomposition of water molecules into hydroxyl radicals. The hydroxyl radicals have high potential to reduce carboxylic or carbonyl groups by eliminating $CO/CO_2$ and $H_2O$, consequently allows restructuration of aromatic carbon structure [34]. The removal of the oxygen functional groups especially at the edges of GO periphery also decreases the *d*-spacing values from 0.80 nm to 0.74 nm as shown in the XRD patterns (Fig. S2).

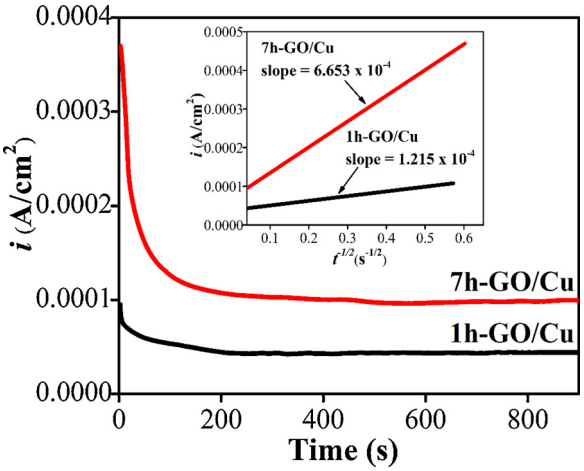


**Fig. 2.** Current-transient (*i vs. t*) curves and (inset) slopes for *i vs.* $t^{-1/2}$ during EPD for 1h-GO/Cu and 7h-GO/Cu.

### 3.2. Characterization of EPD-GO coatings

EPD process of GO can be observed through chronoamperograms as shown in Fig. 2. The figure depicts that the transient current of 7h-GO/Cu is higher than that of 1h-GO/Cu, with total charge value of 0.045 C/cm$^2$ as compared to 0.019 C/cm$^2$ for 1h-GO/Cu (integrated area under the curve). The ratio of diffusion coefficient (*D*) was then estimated by comparing the *i vs.* $t^{-1/2}$ slope (inset Fig. 2) using Cottrell equation (Eq. (1)), where *n*, *F*, *A* and *C* remain constant for both samples.

$$I = \frac{nFACD^{1/2}}{(\pi t)^{1/2}} \quad (1)$$

It is found that *D* for 7h-GO/Cu is 5.5-times higher as compared to 1h-GO/Cu. This explains the higher charge transfer for small size GO sheets may be attributed to the higher diffusion rate. The small size GO sheets are electrophoretically drawn at a faster rate and deposited onto the anode surface. As discussed by Raza et al. [26], partial GO reduction occurs through oxidative decarboxylation process during anodic deposition. Therefore, we suggest that a higher diffusion rate increases the reduction of small size GO sheets as compared to the large size GO sheets. The coating thickness was measured by a surface profiler. It is interesting to note that notwithstanding the higher diffusion rate for smaller GO sheets size, it forms the coating (7h-GO/Cu) with lower thickness (1.52 ± 0.01 µm) as compared to that of the coating from larger GO sheets size (1h-GO/Cu; 3.61 ± 0.02 µm). It proves that for the GO in larger sheets size, there are heavy sheets stacking during coating formation, which may create pinholes for the water permeation during the corrosion process. On the other hand, the thinner 7h-GO/Cu coating also indicates higher compactness of the film with lesser pinholes. The EPD process to form 1h-GO/Cu and 7h-GO/Cu coatings is schematically presented as Fig. 3.

FTIR spectra for the 1h-GO/Cu and 7h-GO/Cu coatings are shown in Fig. 4a. The ORB values were calculated and found to be 0.40 and 0.36 for 1h-GO/Cu and 7h-GO/Cu, respectively. As compared to the ORB before EPD, the lower ORB values for both coatings suggests that the oxidative decarboxylation reduction occurs during EPD process. By

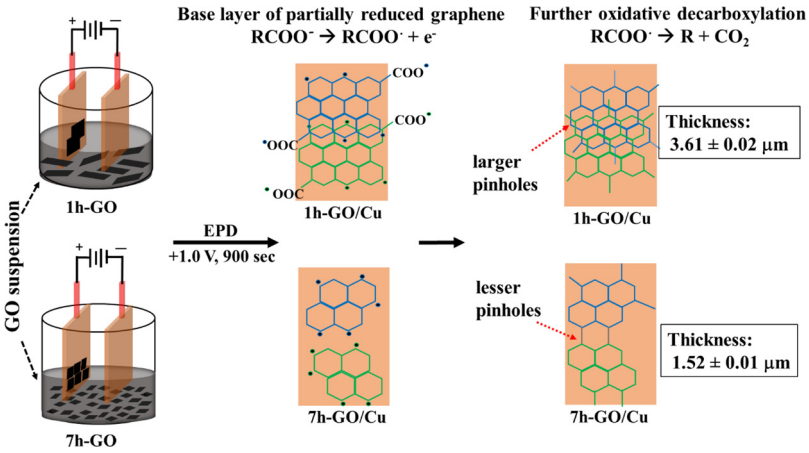


**Fig. 3.** Schematic presentation of EPD coating with larger GO sheets (1h-GO/Cu) and smaller GO sheets (7h-GO/Cu).

comparing the ORB, the percentage of reduction is estimated to be 42.8% and 44.6% for 1h-GO/Cu and 7h-GO/Cu, respectively. The higher percentage of reduction also suggests that more hydrophobic coating is produced in the 7h-GO/Cu. The increased hydrophobicity of 7h-GO/Cu is proven by the wettability measurement where 7h-GO/Cu and 1h-GO/Cu show contact angle of 88.6° and 71.3°, respectively (Fig. S3).

The Raman spectra measured at 532 nm for the coatings are presented in Fig. 4b. At 7h-GO/Cu with smaller GO sheets, there is a slight broadening of the FWHM of *D* peak, indicating that there is an increase of defects or disorder due to the increase of GO edges with size reduction [46,47]. The *D* and *G* bands do not shift as a function of the GO sheets size and $I_D/I_G$ (integrated areas ratio) is slightly different (1.25 for 1h-GO/Cu and 1.35 for 7h-GO/Cu), denoting the fragmentation of GO into smaller sizes does not alter the probability of finding six fold ring on the sheets [34]. The graphene crystallite size, $L_a$ was also estimated from Eq. (2) [48]:

$$L_a = (2.4 \times 10^{-10})\lambda_l^4 \left(I_D/I_G\right)^{-1} \quad (2)$$

where $L_a$ is the crystallite size and $\lambda_l$ is the wavelength of the laser source (nm). The results show that graphene crystallite size for 1h-GO/Cu is larger (15.38 nm) than the graphene crystallite size for 7h-GO/Cu (14.24 nm). This is also consistent with the lateral size distribution findings.

The electron microscopic images in Fig. 5a and b show the surface texture of 1h-GO/Cu and 7h-GO/Cu. The surface texture for 1h-GO/Cu is coarse and rough as compared to that of 7h-GO/Cu. The surface texture was further investigated by AFM as shown in Fig. 5c and d. It is worth noting that the surface roughness, $R_a$ was measured to be 50.21 ± 0.28 and 26.41 ± 0.30 nm for 1h-GO/Cu and 7h-GO/Cu, respectively. Higher surface roughness for 1h-GO/Cu can be associated to the larger sheets size of 1h-GO and the possibility of sheets stacking up during the EPD process [25,26,49]. The findings suggest that 7h-GO/Cu coating is more homogenous and may possess stronger coating adhesion due to the smoother surface coverage. The smoother surface of 7h-GO/Cu also corroborates the higher compactness of the coating. The stronger coating of 7h-GO/Cu is proven by the higher value of Rockwell hardness (HR = 50.6 ± 0.1) as compared to that of 1h-GO/Cu (HR = 39.8 ± 0.1). In addition, upon indentation, 1h-GO/Cu shows a larger area of crack propagation, probably due to the weaker surface adhesion of the coating as shown in Fig. 5e. On the other hand, 7h-GO/Cu shows limited crack propagation, which signifies stronger surface adhesion (Fig. 5f). The higher degree of surface adhesion is crucial in corrosion protection and may reduce water permeation that causes delamination of the coating.

### 3.3. Corrosion performance

The corrosion performance of 1h-GO/Cu and 7h-GO/Cu coatings were evaluated using the potentiodynamic polarization method in a 3.5% NaCl solution. The Tafel polarization plot in Fig. 6 shows that the corrosion potential, $E_{corr}$ for 7h-GO/Cu is shifted towards positive direction at -0.161 V as compared to -0.188 V for 1h-GO/Cu. The corrosion current, $I_{corr}$ is found to be 0.0869 μA/cm$^2$ for 7h-GO/Cu and 0.1245 μA/cm$^2$ for 1h-GO/Cu. The higher positive value of $E_{corr}$ and lower value of $I_{corr}$ denote better corrosion resistance of 7h-GO/Cu. The corrosion rate (CR) was calculated from the corrosion current values using the previous equation [50]. The CR of 1h-GO/Cu and 7h-GO/Cu were computed to be 0.0572 mpy and 0.0399 mpy, respectively. This observation manifests that the GO sheets in smaller size form a stronger

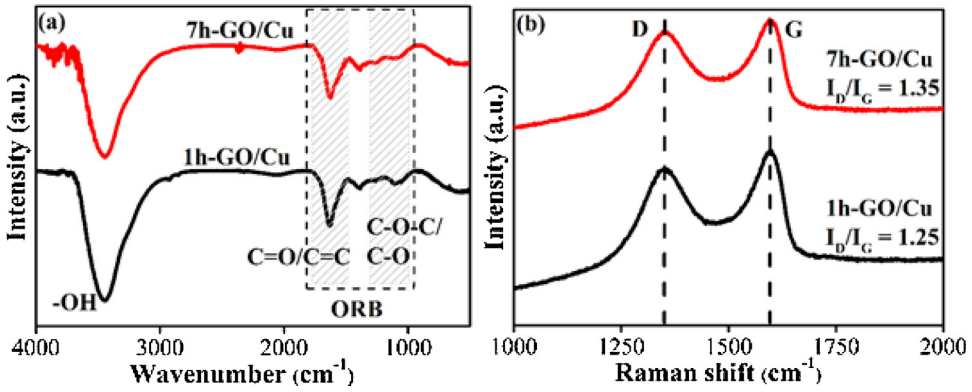


**Fig. 4.** (a) FTIR spectra showing the area of ORB and (b) Raman spectra with the $I_D/I_G$ ratio for the 11h-GO/Cu and 7h-GO/Cu coatings, respectively.

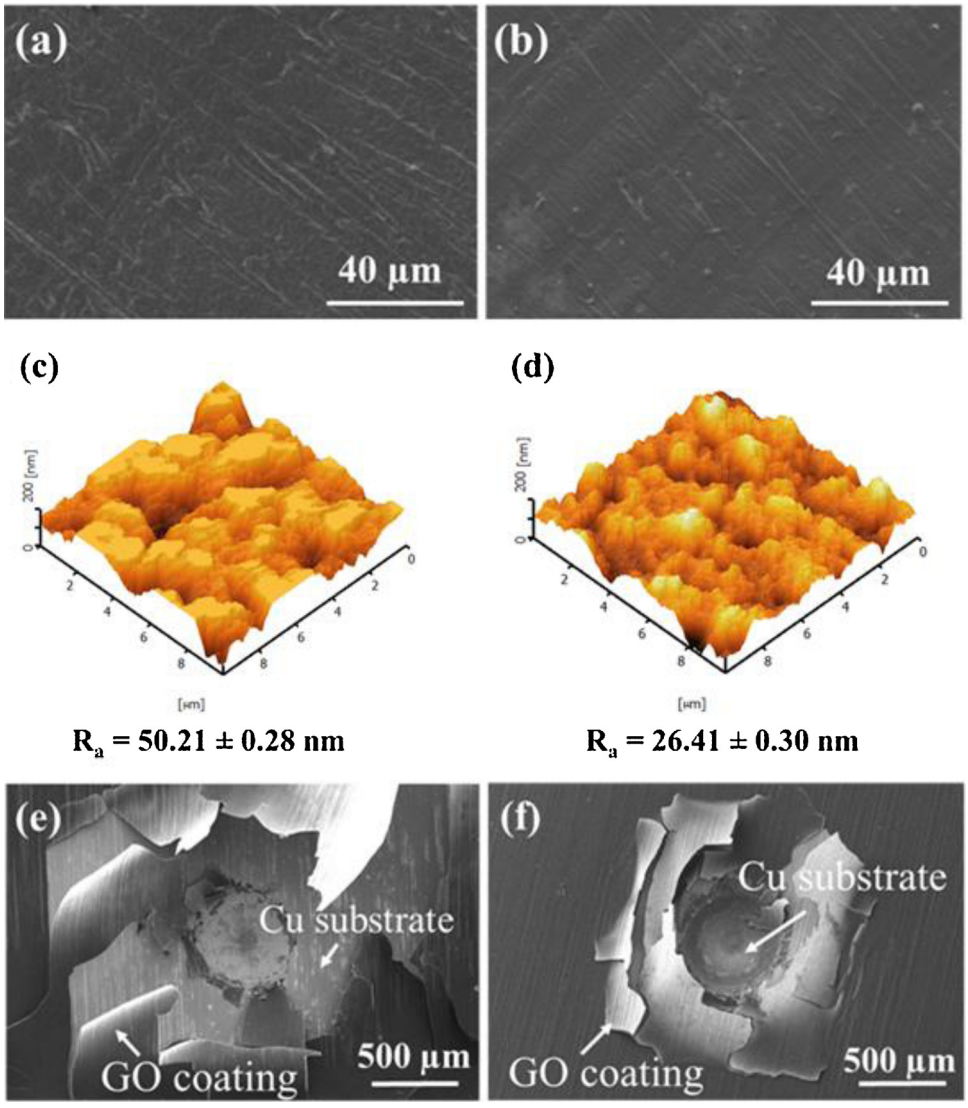


**Fig. 5.** (a, d) SEM, (c, d) AFM images showing surface texture and surface roughness, $R_a$ for 1h-GO/Cu and 7h-GO/Cu and (e, f) shows the indentation and crack area for 1h-GO/Cu and 7h-GO/Cu, respectively.

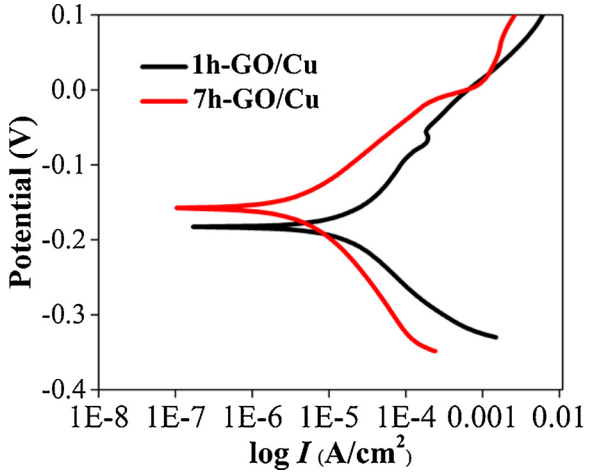


**Fig. 6.** Tafel plots for 1h-GO/Cu and 7h-GO/Cu studied in 3.5% NaCl electrolyte solution.

passivation coating towards corrosion due to its impermeability towards water molecules. As proven from the structural characterization findings, the higher reduction of 7h-GO/Cu renders a coating with lesser oxygen functional groups and higher hydrophobicity, which effectively obstructs water permeation through the coating for corrosion initiation. In addition, the 7h-GO/Cu coating is more compact with lesser pinholes for water permeation. Further protection ability and its mechanism were further investigated by EIS approach.

### 3.4. Time-based electrochemical analysis

The EIS analysis begins with Nyquist plots (Fig. 7a) and their equivalent circuit (Fig. 7b). The fitted circuit parameters are tabulated in Table 1, where $R_s$ is electrolyte resistance, $R_{pore}$ is pore resistance, $R_{ct}$ is charge transfer resistance, $CPE_c$ is constant phase element for coating and $CPE_{dl}$ is constant phase element for electric double layer. The CPE is used instead of pure capacitance in the circuit as non-ideal capacitance behavior was observed due to the diffusion phenomenon [51]. It is obvious that 7h-GO/Cu possesses higher $R_{pore}$ and $R_{ct}$ values, to show the higher corrosion resistance behavior, which is coherent to the Tafel analysis. It has been found that the $R_{pore}$ value for 7h-GO/Cu is approximately 2-times higher than that of 1h-GO/Cu which can be

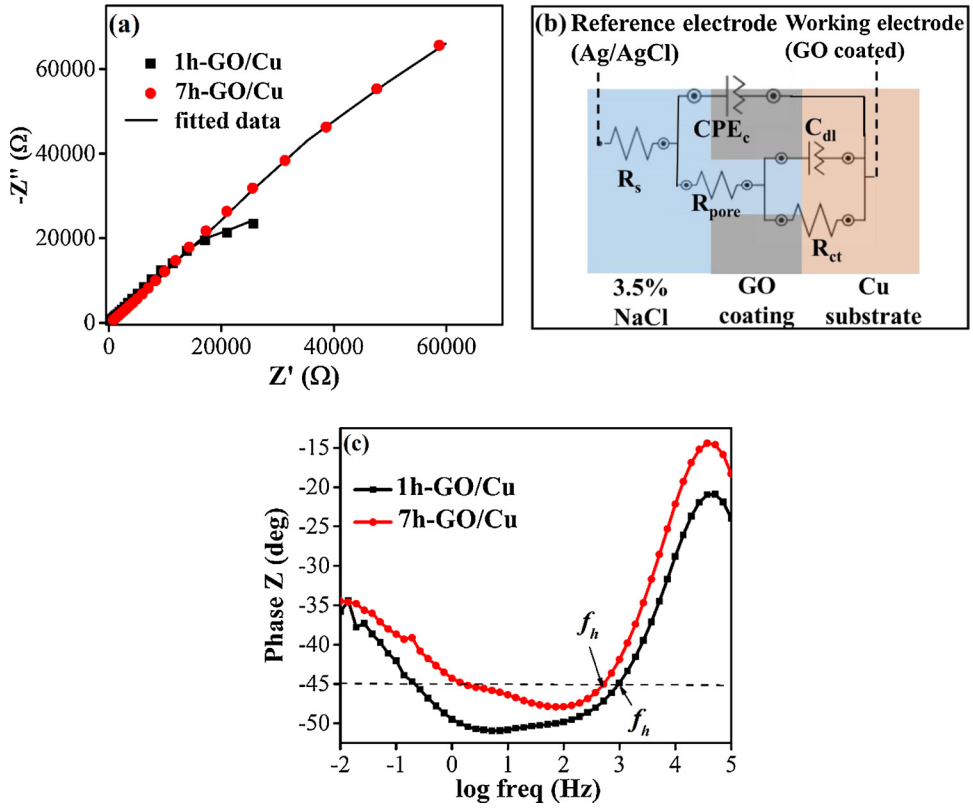


**Fig. 7.** (a) Nyquist plots of 1h-GO/Cu and 7h-GO/Cu coatings at the onset of exposure ($t$ = 0 h); (b) the electrochemical equivalent circuit used to simulate the experimental data; (c) Bode phase plots of 1h-GO/Cu and 7h-GO/Cu at the onset of exposure ($t$ = 0 h).

**Table 1**
The circuit fitting parameters for 1h-GO/Cu and 7h-GO/Cu coatings.

| Sample | $R_s$ (Ω) | $R_{pore}$ (kΩ) | $R_{ct}$ (MΩ) | $CPE_c$ ($\mu\Omega^{-1}$ $cm^{-2}$ $s$) | $CPE_{dl}$ ($\mu\Omega^{-1}$ $cm^{-2}$ $s$) |
|---|---|---|---|---|---|
| 1h-GO/Cu | 632 | 3.46 | 1.55 | 1.68 | 1.46 |
| 7h-GO/Cu | 600 | 6.80 | 1.92 | 1.11 | 1.81 |

attributed to the higher hydrophobicity and compact coating, which obstructs water permeation. Meanwhile, higher $R_{ct}$ value for 7h-GO/Cu denotes that the coating successfully reduces the anodic reaction in the corrosion process, thereby protecting the underlying Cu.

Fig. 7c shows the Bode plots for 1h/GO/Cu and 7h-GO/Cu. The high breakpoint frequency ($f_h$) which indicates the capacitive and resistive transition boundary can be deduced from the Bode plots, and it is independent of the substrate [52]. The $f_h$ is the highest frequency at 45° phase angle [53], and it can be correlated to the electrochemically active area by Eq. (3) [54]:

$$f_h = \frac{1}{2\pi\varepsilon\varepsilon_o\rho_o}\frac{A}{A_o} \quad (3)$$

where $A_o$ and $A$ are the total exposed coating area and electrochemically active area respectively, $\rho_o$ is the pores resistivity, and $\varepsilon$ and $\varepsilon_o$ are the dielectric constants for the coating saturated with water and permittivity of free space, respectively. It can be seen that the higher $f_h$ for 1h-GO/Cu denotes the higher electrochemically active area ratio ($A/A_o$), which indicates higher corrosion activity for 1h-GO/Cu.

The coating corrosion behavior was then studied over a long exposure time (up to 336 h) in the same electrolyte. The Bode and Nyquist plots for 1h-GO/Cu and 7h-GO/Cu at different immersion time are shown in Fig. S4a-4d. The $f_h$ values at different immersion time are obtained from the Bode plots and presented as Fig. 8a. It can be clearly seen that the $f_h$ values shift towards higher frequency with the increase of immersion time for all samples. It signifies the corrosion activity increases with longer immersion time. It is worth noting that the $f_h$ for 1h-GO/Cu is higher than that of 7h-GO/Cu at any immersion time, which indicates GO with smaller sheets size could form the coating (7h-GO/Cu) with lower corrosion activity. Fig. 8b depicts the $R_{pore}$ as a function of immersion time. It is obvious that both 1h-GO/Cu and 7h-GO/Cu coatings show the decreasing trend of $R_{pore}$ for longer immersion time, which could be related to the water permeation into the coatings. Apparently, the $R_{pore}$ values approach saturation at 240–336 h implying that water thoroughly penetrates the coatings and possibly occupying all the pinholes. Interestingly, the $R_{pore}$ values for 7h-GO/Cu are higher than that of 1h-GO/Cu at any immersion time, suggesting coating from smaller GO sheets size is more resistive towards water permeation, which can also be related to its compactness and hydrophobic surface.

The water permeation in the coatings was evaluated by measuring the changes in the electrical capacitance of the coating. It is well known that the capacitance is directly proportional to the dielectric constant, where the dielectric constant of the coating can be increased by water permeation into the coatings. In this study, the CPE values are converted into effective capacitance, $C_{eff}$, using Eq. (4) [55]:

$$C_{eff} = Q^{1/n}R_{pore}^{(1-n)/n} \quad (4)$$

where $n$ is the CPE parameter. Fig. 9a shows that the $C_{eff}$ values are low at $t$ = 0 for both coatings, indicating an intact barrier coating for water permeation. However, $C_{eff}$ values increase with immersion time, corresponding to the water permeation in both coatings over time. The $C_{eff}$ for 1h-GO/Cu is higher than that of 7h-GO/Cu, which indicates more water permeates into the coating formed by larger GO sheets size. The results are in agreement with the quantification of water uptake in the coatings as evident in Fig. 9b. The water uptake is calculated using Eq. (5) derived by Brasher and Kingsbury [21]:

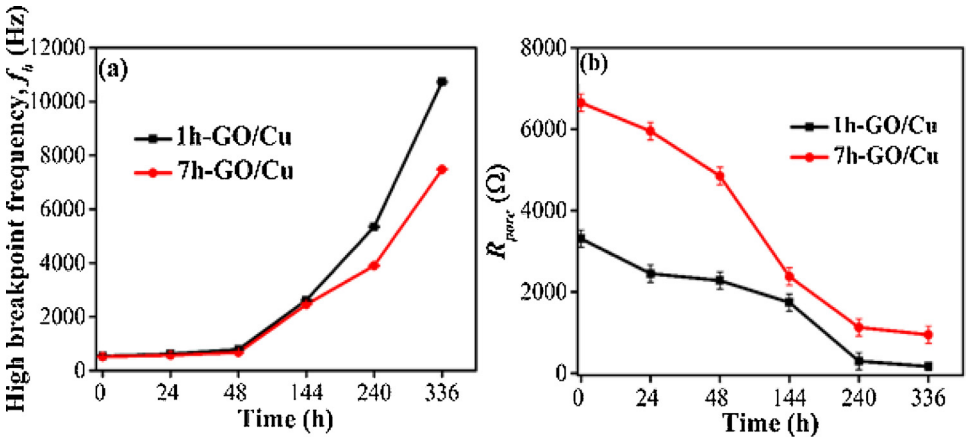


**Fig. 8.** (a) High breakpoint frequency, $f_h$ and (b) $R_{pore}$ values as a function of time for 1 h-GO/Cu and 7h-GO/Cu.

$$X_v\,(by\,\%\,volume) = \frac{\log\frac{C_t}{C_o}}{\log\varepsilon_{H_2O}} \times 100 \tag{5}$$

$X_v$ denotes the percentage of water absorbed in the coating, $C_o$ is the initial coating capacitance ($t = 0$), $C_t$ is the measured coating capacitance at $t$ time and $\varepsilon_{H_2O}$ is the relative dielectric constant of water. It can be concluded that the higher amount of water is absorbed by the 1h-GO/Cu coating as compared to that of 7h-GO/Cu, which could be associated to the higher oxygen functional groups on the 1 h-GO/Cu that provide permeation pathway for water molecules. Higher water absorption in 1h-GO/Cu is also corroborated by the coating peeling off after 336 h of immersion, as evident by the Fig. S5 where 7h-GO/Cu is still showing visibly intact coating.

The kinetics of water absorption into the coating was further investigated by measuring its diffusion coefficient in the coating ($D_{coating}$). The value of $D_{coating}$ can be obtained from Eq. (6):

$$\frac{\log\frac{C_t}{C_o}}{\log\frac{C_s}{C_o}} = \frac{4\sqrt{D}}{L\sqrt{\pi}}\sqrt{t} \tag{6}$$

where $C_s$ is the capacitance value when the saturated stage is achieved, $D_{coating}$ is the water diffusion coefficient in the coating, $L$ is the coating thickness, and $t$ is the time of measurement. The component on the left side of the equation refers to dimensionless film capacitance (DFC). When water diffusion in the coating approaches ideal Fickian behavior, its $D_{coating}$ can be deduced from the slope of DFC linear response towards $t^{1/2}$ [54]. As shown in Fig. 10, the water diffusion in the coating formed from larger GO sheets size (1 h-GO/Cu) is approximately 8-times higher than that of the coating formed from smaller GO sheets size (7h-GO/Cu). These findings explain that the higher corrosion resistance of coating formed from smaller GO sheets size is predominantly

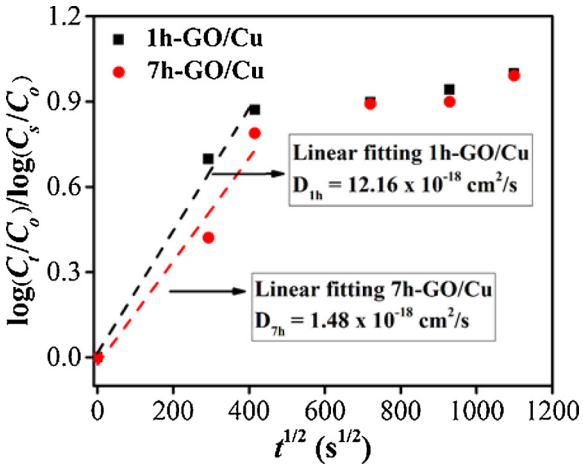


**Fig. 10.** Dimensionless film capacitance (DFC) *vs.* $t^{1/2}$ and linear fitting of initial points for the calculation of diffusion coefficient.

originated from the lower water diffusion in the coating. Again, such low water diffusion rate can be associated to the compact coating with higher hydrophobicity. The diffusion coefficient can be related to the activation energy ($E_A$) by Arrhenius law as stated in Eq. (7) [56]:

$$D = A\exp\left(-\frac{E_A}{RT}\right) \tag{7}$$

$A$ is the Arrhenius constant, $E_A$ is the activation energy for the diffusion process, $T$ is the temperature and $R$ is the gas constant. From the thermodynamics perspective, it can be deduced that 7h-GO/Cu has a higher activation energy of water diffusion (since the temperature is

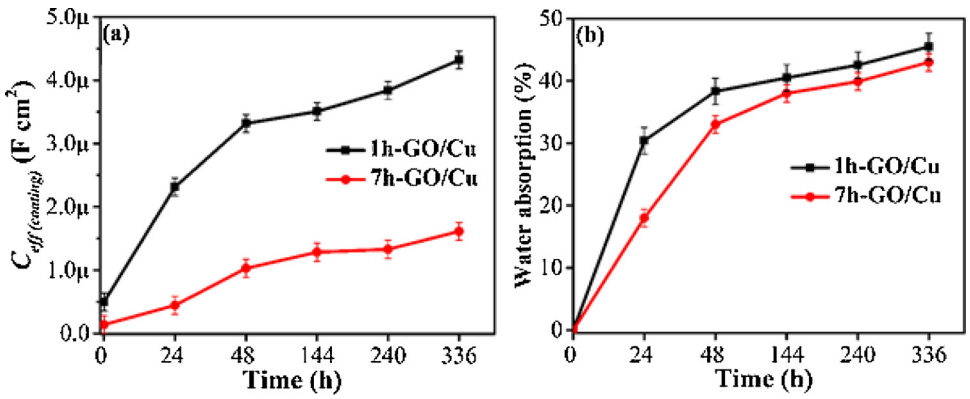


**Fig. 9.** (a) $C_{eff\ (coating)}$ and (b) water absorption (%) as a function of time for 1h-GO/Cu and 7h-GO/Cu.

same for all testing), thereby acts as a restricting force against water permeation and the onset of the corrosion process.

## 4. Conclusions

This study reports on the coating formed from smaller GO sheets size (mean lateral size of 100 nm) provides better corrosion resistance behavior. It is interesting to note that the small size GO sheets diffuse faster during EPD process, to form thinner and compact coating (1.52 ± 0.01 μm) with higher oxygen groups reduction. The EPD coating formed from smaller GO sheets size provides higher corrosion resistance with CR of 0.0399 mpy as compared to the coating form from larger GO sheets size (CR of 0.0572 mpy). EIS analysis suggests that lower water permeation is found on the coating formed from smaller GO sheets size, which is compact and more hydrophobic. All these properties effectively increase activation energy for water permeation into the coating, reduce water diffusion rate in the coating and hence create a tortuous pathway for water molecules from reaching the underlying copper substrate for corrosion process.

## Conflict of interest

The authors declare no competing financial interest.

## Data availability

The raw/processed data required to reproduce these findings cannot be shared at this time as the data also forms part of an ongoing study.

## Acknowledgments

The authors would like to acknowledge the funding from the Ministry of Education Malaysia in the form of [RDU170113: FRGS/1/2017/STG07/UMP/01/1] and Universiti Malaysia Pahang grant RDU170357. Moreover, the authors extend their appreciation to King Khalid University, the Ministry of Education – Kingdom of Saudi Arabia for supporting this research through a grant (RCAMS/KKU/002-18) under research center for advanced material science.

## Appendix A. Supplementary data

Supplementary material related to this article can be found, in the online version, at doi:https://doi.org/10.1016/j.porgcoat.2019.05.011.

## References

[1] P.B. Raja, M. Ismail, S. Ghoreishiamiri, J. Mirza, M.C. Ismail, S. Kakooei, A.A. Rahim, Reviews on corrosion inhibitors: a short view, Chem. Eng. Commun. 203 (2016) 1145–1156.
[2] X. Luo, S. Yuan, X. Pan, C. Zhang, S. Du, Y. Liu, Synthesis and enhanced corrosion protection performance of reduced graphene oxide nanosheet/ZnAl layered double hydroxide composite films by hydrothermal continuous flow method, ACS Appl. Mater. Interfaces 9 (2017) 18263–18275.
[3] H. Zheng, M. Guo, Y. Shao, Y. Wang, B. Liu, G. Meng, Graphene oxide–poly(urea–formaldehyde) composites for corrosion protection of mild steel, Corros. Sci. 139 (2018) 1–12.
[4] N. M'hiri, D. Veys-Renaux, E. Rocca, I. Ioannou, N.M. Boudhrioua, M. Ghoul, Corrosion inhibition of carbon steel in acidic medium by orange peel extract and its main antioxidant compounds, Corros. Sci. 102 (2016) 55–62.
[5] N. Odewunmi, S. Umoren, Z. Gasem, Utilization of watermelon rind extract as a green corrosion inhibitor for mild steel in acidic media, J. Ind. Eng. Chem. 21 (2015) 239–247.
[6] M. Mobin, M. Rizvi, Polysaccharide from Plantago as a green corrosion inhibitor for carbon steel in 1 M HCl solution, Carbohydr. Polym. 160 (2017) 172–183.
[7] M.A. Chidiebere, E.E. Oguzie, L. Liu, Y. Li, F. Wang, Ascorbic acid as corrosion inhibitor for Q235 mild steel in acidic environments, J. Ind. Eng. Chem. 26 (2015) 182–192.
[8] M. Winnicki, A. Małachowska, A. Baszczuk, M. Rutkowska-Gorczyca, D. Kukla, M. Lachowicz, A. Ambroziak, Corrosion protection and electrical conductivity of copper coatings deposited by low-pressure cold spraying, Surf. Coat. Technol. 318 (2017) 90–98.
[9] O. Oladijo, M. Mathabatha, T. Ntsoane, Characterization and corrosion behaviour of plasma sprayed Zn-Sn alloy coating on mild steel, Surf. Coat. Technol. 352 (2018) 654–661.
[10] X. Xu, L. Zhu, W. Li, H. Liu, A variable hydrophobic surface improves corrosion resistance of electroplating copper coating, Appl. Surf. Sci. 257 (2011) 5524–5528.
[11] L. Besra, M. Liu, A review on fundamentals and applications of electrophoretic deposition (EPD), Prog. Mater. Sci. 52 (2007) 1–61.
[12] A. Chavez, M.S. Shaffer, A.R. Boccaccini, Applications of graphene electrophoretic deposition. A review, J. Phys. Chem. B 117 (2012) 1502–1515.
[13] Y. Ma, J. Han, M. Wang, X. Chen, S. Jia, Electrophoretic deposition of graphene-based materials: a review of materials and their applications, J. Materiomics 4 (2018) 108–120.
[14] Y. Tong, S. Bohm, M. Song, Graphene based materials and their composites as coatings, Austin J. Nanomed. Nanotechnol. 1 (2013) 1003–1019.
[15] A. Jabbar, G. Yasin, W.Q. Khan, M.Y. Anwar, R.M. Korai, M.N. Nizam, G. Muhyodin, Electrochemical deposition of nickel graphene composite coatings: effect of deposition temperature on its surface morphology and corrosion resistance, RSC Adv. 7 (2017) 31100–31109.
[16] N. Li, L. Zhang, M. Xu, T. Xia, X. Ruan, S. Song, H. Ma, Preparation and mechanical property of electrodeposited Al-graphene composite coating, Mater. Des. 111 (2016) 522–527.
[17] C.P. Kumar, T. Venkatesha, R. Shabadi, Preparation and corrosion behavior of Ni and Ni–graphene composite coatings, Mater. Res. Bull. 48 (2013) 1477–1483.
[18] S. Lee, M. Cho, H. Lee, L. Pu, Y. Lee, Electrodeposition of graphene layers doped with Brønsted acids, J. Mater. Sci. 48 (2013) 6891–6896.
[19] S. Mukherjee, Z. Ren, G. Singh, Beyond graphene anode materials for emerging metal ion batteries and supercapacitors, Nano-Micro Lett. 10 (2018) 70.
[20] D.W. Johnson, B.P. Dobson, K.S. Coleman, A manufacturing perspective on graphene dispersions, Curr. Opin. Colloid Interface Sci. 20 (2015) 367–382.
[21] D. Brasher, A. Kingsbury, Electrical measurements in the study of immersed paint coatings on metal. I. Comparison between capacitance and gravimetric methods of estimating water-uptake, J. Appl. Chem. 4 (1954) 62–72.
[22] S. Qiu, W. Li, W. Zheng, H. Zhao, L. Wang, Synergistic effect of polypyrrole-intercalated graphene for enhanced corrosion protection of aqueous coating in 3.5% NaCl solution, ACS Appl. Mater. Interfaces 9 (2017) 34294–34304.
[23] G. Eda, M. Chhowalla, Chemically derived graphene oxide: towards large-area thin-film electronics and optoelectronics, Adv. Mater. 22 (2010) 2392–2415.
[24] Y. Wu, X. Zhu, W. Zhao, Y. Wang, C. Wang, Q. Xue, Corrosion mechanism of graphene coating with different defect levels, J. Alloys. Compd. 777 (2019) 135–144.
[25] S.J. An, Y. Zhu, S.H. Lee, M.D. Stoller, T. Emilsson, S. Park, A. Velamakanni, J. An, R.S. Ruoff, Thin film fabrication and simultaneous anodic reduction of deposited graphene oxide platelets by electrophoretic deposition, J. Phys. Chem. Lett. 1 (2010) 1259–1263.
[26] M.A. Raza, Z.U. Rehman, F.A. Ghauri, A. Ahmad, R. Ahmad, M. Raffi, Corrosion study of electrophoretically deposited graphene oxide coatings on copper metal, Thin Solid Films 620 (2016) 150–159.
[27] C.-Y. Ho, S.-M. Huang, S.-T. Lee, Y.-J. Chang, Evaluation of synthesized graphene oxide as corrosion protection film coating on steel substrate by electrophoretic deposition, Appl. Surf. Sci. 477 (2019) 226–231.
[28] J.H. Park, J.M. Park, Electrophoretic deposition of graphene oxide on mild carbon steel for anti-corrosion application, Surf. Coat. Technol. 254 (2014) 167–174.
[29] M.A. Raza, A. Ali, F.A. Ghauri, A. Aslam, K. Yaqoob, A. Wasay, M. Raffi, Electrochemical behavior of graphene coatings deposited on copper metal by electrophoretic deposition and chemical vapor deposition, Surf. Coat. Technol. 332 (2017) 112–119.
[30] A. Bellunato, H. Arjmandi Tash, Y. Cesa, G.F. Schneider, Chemistry at the edge of graphene, ChemPhysChem 17 (2016) 785–801.
[31] W. Yuan, Y. Zhou, Y. Li, C. Li, H. Peng, J. Zhang, Z. Liu, L. Dai, G. Shi, The edge-and basal-plane-specific electrochemistry of a single-layer graphene sheet, Sci. Rep. 3 (2013) 2248–2255.
[32] X. Qi, T. Zhou, S. Deng, G. Zong, X. Yao, Q. Fu, Size-specified graphene oxide sheets: ultrasonication assisted preparation and characterization, J. Mater. Sci. 49 (2014) 1785–1793.
[33] J. Kim, S.W. Kim, H. Yun, B.J. Kim, Impact of size control of graphene oxide nanosheets for enhancing electrical and mechanical properties of carbon nanotube–polymer composites, RSC Adv. 7 (2017) 30221–30228.
[34] G. Gonçalves, M. Vila, I. Bdikin, A. De Andrés, N. Emami, R.A. Ferreira, L.D. Carlos, J. Grácio, P.A. Marques, Breakdown into nanoscale of graphene oxide: confined hot spot atomic reduction and fragmentation, Sci. Rep. 4 (2014) 6735–6743.
[35] E.T.Y. Lih, T.L. Ling, K.F. Chong, Facile corrosion protection coating from graphene, Int. J. Chem. Eng. Appl. 3 (2012) 453–455.
[36] B.P. Singh, S. Nayak, K.K. Nanda, B.K. Jena, S. Bhattacharjee, L. Besra, The production of a corrosion resistant graphene reinforced composite coating on copper by electrophoretic deposition, Carbon 61 (2013) 47–56.
[37] G.A.M. Ali, S.A. Makhlouf, M.M. Yusoff, K.F. Chong, Structural and electrochemical characteristics of graphene nanosheets as supercapacitor electrodes, Rev. Adv. Mater. Sci. 40 (2015) 35–43.
[38] H. Xu, K.S. Suslick, Sonochemical preparation of functionalized graphenes, J. Am. Chem. Soc. 133 (2011) 9148–9151.
[39] C. Botas, A.M. Pérez-Mas, P. Álvarez, R. Santamaría, M. Granda, C. Blanco, R. Menéndez, Optimization of the size and yield of graphene oxide sheets in the exfoliation step, Carbon 63 (2013) 576–578.
[40] S. Pan, I.A. Aksay, Factors controlling the size of graphene oxide sheets produced via the graphite oxide route, ACS Nano 5 (2011) 4073–4083.
[41] C.-Y. Su, Y. Xu, W. Zhang, J. Zhao, X. Tang, C.-H. Tsai, L.-J. Li, Electrical and spectroscopic characterizations of ultra-large reduced graphene oxide monolayers,

Chem. Mater. 21 (2009) 5674–5680.
[42] M. Cai, D. Thorpe, D.H. Adamson, H.C. Schniepp, Methods of graphite exfoliation, J. Mater. Chem. 22 (2012) 24992–25002.
[43] G.-Q. Qi, J. Cao, R.-Y. Bao, Z.-Y. Liu, W. Yang, B.-H. Xie, M.-B. Yang, Tuning the structure of graphene oxide and the properties of poly(vinyl alcohol)/graphene oxide nanocomposites by ultrasonication, J. Mater. Chem. A 1 (2013) 3163–3170.
[44] K. Haruna, T.A. Saleh, I.B. Obot, S.A. Umoren, Cyclodextrin-based functionalized graphene oxide as an effective corrosion inhibitor for carbon steel in acidic environment, Prog. Org. Coat. 128 (2019) 157–167.
[45] J. Guerrero-Contreras, F. Caballero-Briones, Graphene oxide powders with different oxidation degree, prepared by synthesis variations of the Hummers method, Mater. Chem. Phys. 153 (2015) 209–220.
[46] B.W.N.H. Hemasiri, J.-K. Kim, J.-M. Lee, Synthesis and characterization of graphene/ITO nanoparticle hybrid transparent conducting electrodeElectrode, Nano-Micro Lett. 10 (2017) 18.
[47] Y. Zhao, X. Li, M. Wang, L. Zhang, B. Chu, C. Yang, Y. Liu, D. Zhou, Y. Lu, Constructing sub-10-nm gaps in graphene-metal hybrid system for advanced surface-enhanced Raman scattering detection, J. Alloys Compd. 720 (2017) 139–146.
[48] F. Tuinstra, J.L. Koenig, Raman spectrum of graphite, J. Chem. Phys. 53 (1970) 1126–1130.
[49] S. Hong, S. Jung, S. Kang, Y. Kim, X. Chen, S. Stankovich, S.R. Ruoff, S. Baik, Dielectrophoretic deposition of graphite oxide soot particles, J. Nanosci. Nanotechnol. 8 (2008) 424–427.
[50] Y. Wei, J. Wang, X. Jia, Electrochemical Studies of Corrosion Inhibiting Effect of Polyaniline Coatings, American Chemical Society, Washington, DC (United States), United States, 1995.
[51] C. Hsu, F. Mansfeld, Concerning the conversion of the constant phase element parameter Y0 into a capacitance, Corrosion 57 (2001) 747–748.
[52] H.P. Hack, J.R. Scully, Defect area determination of organic coated steels in seawater using the breakpoint frequency method, J. Electrochem. Soc. 138 (1991) 33–40.
[53] S. Haruyama, S. Sudo, Electrochemical impedance for a large structure in soil, Electrochim. Acta 38 (1993) 1857–1865.
[54] Z. Feng, G. Frankel, Evaluation of coated Al alloy using the breakpoint frequency method, Electrochim. Acta 187 (2016) 605–615.
[55] B. Hirschorn, M.E. Orazem, B. Tribollet, V. Vivier, I. Frateur, M. Musiani, Determination of effective capacitance and film thickness from constant-phase-element parameters, Electrochim. Acta 55 (2010) 6218–6227.
[56] S. Downey, O. Devereux, The use of impedance spectroscopy in evaluating moisture-caused failure of adhesives and paints, Corrosion 45 (1989) 675–684.